AIAA SciTech
13-17 January 2014, National Harbour, Maryland
52nd AIAA Aerospace Sciences Meeting

AIAA 2014-0225

Hybrid RANS-LES Modeling Using a Low-Reynolds-Number $k-\omega$ Based Model

Sebastian Arvidson[1,2*†]

[1] *Department of Applied Mechanics, Chalmers University of Technology, SE-412 96, Gothenburg, SWEDEN*

[2] *SAAB AB, Aeronautics, SE-582 88, Linköping, SWEDEN*

Lars Davidson[3‡]

[3] *Department of Applied Mechanics, Chalmers University of Technology, SE-412 96, Gothenburg, SWEDEN*

Shia-Hui Peng[3,4‡]

[4] *FOI, Swedish Defence Research Agency, SE-164 90, Stockholm, SWEDEN*

Hybrid RANS-LES modeling is proposed using a Low-Reynold-Number (LRN) $k-\omega$ model. The model is demonstrated in a zonal RANS-LES approach and in an embedded LES approach. The model is calibrated and evaluated using Decaying Homogeneous Isotropic Turbulence (DHIT), turbulent channel flow and turbulent flow over a hump. The effect of different LES length scales on log-layer mismatch and turbulence resolving capability is demonstrated using the proposed model. Interface conditions are proposed in the embedded LES approach in order to reduce the grey area zone in the LES domain downstream of the RANS region. To further improve the development of turbulence resolving flow in the LES region downstream of the interface, anisotropic turbulent velocity fluctuations from synthetic turbulence are added. The hybrid RANS-LES modeling approaches that are presented, using the LRN $k-\omega$ based model, show that predictions of turbulence resolving flows are in reasonable agreement with experimental data and DNS data. Moreover, the choice of the LES length scale using the proposed model is shown to be of great importance in reducing the log-layer mismatch.

I. Introduction

The Low-Reynolds-Number $k-\omega$ model by Peng et al.[1] (hereafter the PDH-LRN model) was recently used in transonic duct flow and produced good results.[2] The reported flow case involves shock/boundary-layer interaction (SBLI) and local recirculation zones at the shock in the corners of the rectangular duct. The study made a comparison of several models, including Reynolds-Average Navier-Stokes (RANS) models and turbulence resolving approaches. Most of the models had problems in accurately predicting the onset of the separation bubble caused by the shock due to an inaccurately predicted incoming boundary layer. It was concluded that near-wall modeling is essential for the studied flow case to deal with the SBLI and consequent flow phenomena including the local recirculation bubble. Of the models used in the study, the PDH-LRN model was the only one able to appropriately represent the flow field.

Taking a step towards improved hybrid RANS-LES modeling, the PDH-LRN model seems to be suitable as base model for shallow type separation flows. The PDH-LRN model is designed and intended for internal flows with local flow separations, which is preferable since the proposed modeling approaches are intended

*PhD. student, Department of Applied Mechanics, Chalmers University of Technology
†Systems Engineer, Propulsion Aerodynamics and Performance, SAAB AB, Aeronautics
‡Professor, Department of Applied Mechanics, Chalmers University of Technology,

for internal flows involving large-scale turbulence, such as compact inlet ducts on low observable UAVs and fighter aircrafts.

In the case of hybrid RANS-Large Eddy Simulation (LES) modeling of attached boundary layer flows, where the intention is to simulate only the inner part of the boundary layer using RANS, a fast development of the turbulence-resolving flow in the LES region, after switching from RANS to LES, is essential in order to minimize the log-layer mismatch. Turning to shallow type flow separations, the oncoming boundary layer and the resolved boundary layer turbulence are important factors for accurately predicting the flow separation. In both the cases of log-layer mismatch and shallow type separations, the LES length scale is an important parameter and is investigated in this paper for high Reynolds number channel flow.

Moreover, the motivation for various length-scale formulations stems from different needs and is dependent on the flow condition considered. Using different length scale formulations can significantly affect the level of turbulence viscosity produced by the model and hence its capability to resolve turbulence.

As motivated by Spalart et al.[3] in the formulation of DES, Δ_{max} (Eq. 1) is chosen in order to protect the boundary layer from LES content and to reduce the risk for Modeled-Stress Depletion (MSD) and Grid Induced Separation (GIS).

$$\Delta_{max} = \max\left(\Delta_x, \Delta_y, \Delta_z\right) \tag{1}$$

Another commonly used length scale, especially in pure LES models, is based on the cubic root of the control volume (Eq. 2). Consequently, due to the subgrid scale turbulent viscosity - filter-width relation, the use of Δ_{max} on stretched grids will produce higher levels of turbulent viscosity compared to Δ_{vol}. This issue was advocated by Breuer et al.[4] in DES simulations over a flat plate at high incidence. However, the use of Δ_{vol} has also been criticized due to its weak physical interpretation.[5]

$$\Delta_{vol} = \left(\Delta_x \Delta_y \Delta_z\right)^{1/3} \tag{2}$$

Davidson and Peng[6] also demonstrated the effect of a different filter width in their zonal formulation. They motivated their choice of the minimum cell size, $\Delta = \min\left(\Delta_x, \Delta_y, \Delta_z\right)$, instead of Δ_{vol} by considerably better performance in channel flow.

Ideally, in off-wall regions and in separated flows, uniform cells should be used, giving $\Delta_{max} = \Delta_{vol}$. However, it is not always possible to form uniform cells in practical engineering flows, e.g. in plane free shear layers, due to the high computational cost. Given a structured grid and that $\Delta = \Delta_{max}$, at the trailing edge of the flat plate where the boundary layers emerge and form the free shear layer, the constraint is often set by the spanwise resolution. The streamwise resolution is adapted to capture the streamwise velocity gradients $\partial U/\partial y$. Moreover, the resolution in the y-direction is a heritage from the wall normal boundary layer resolution.

For plane free shear layers, the grey area problem can be significant because of excessive turbulent viscosity. With free shear layers in mind, Chauvet et al.[7] proposed a length scale based on the direction of the spin axis of the local vorticity. In principal, the length scale is defined by the plane perpendicular to this spin axis of the local vorticity. Thus, the length scale is adapted to the flow field and is only as large as needed to resolve the local vorticity field, giving a minimum of excess turbulent viscosity. Moreover, Deck[8] showed the advantage of using Δ_Ω in free shear flow.

$$\Delta_\Omega = \sqrt{N_x^2 \Delta y \Delta z + N_y^2 \Delta x \Delta z + N_z^2 \Delta x \Delta y} \tag{3}$$

$$\boldsymbol{N} = \frac{\boldsymbol{\Omega}}{\parallel \boldsymbol{\Omega} \parallel}, \qquad \boldsymbol{\Omega} = \nabla \times \boldsymbol{u}$$

The length scales formulations presented in Eq. 2 and 3 reduce the subgrid scale turbulent viscosity on stretched grids compared to Δ_{max}. Such a reduction also reduces the model's resistance to MSD/GIS. For hybrid RANS-LES applications, modifications of the LES length scale must therefore be made carefully. The DDES[9] approach is based on the maximum cell spacing. To reduce the grey area, Deck[8] proposed a combination of the vorticity based length scale and the local maximum cell size. By using the f_d function and introducing a threshold value into f_d, Δ_{max} is used below this value and Δ_Ω above. Due to the lower turbulent viscosity produced with Δ_Ω on stretched grids and because Δ_{max} is not used in the outer part of the boundary layer, Deck's[8] formulation will switch from RANS to LES slightly closer to the wall than the original DDES formulation but with a reduced grey area.

Special attention must be paid to the length scale used in pure LES models or WMLES models, such as the IDDES proposed by Shur et al.[10] According to Shur et al., not only the cell size should be included in a proper LES length scale for down-to-the-wall integration, but also the wall distance, to include the wall proximity effects. In the near wall region, the flow properties should depend only on the wall parallel cell measures, while the free flow should return the standard DES length scale in its LES mode, i.e. $\Delta = \Delta_{max}$. In between the two limits, the length scale should depend on the wall distance.

$$\Delta_{dw} = \min\left(\max\left[C_w d_w, C_w \Delta_{max}, \Delta_{nstep}\right], \Delta_{max}\right) \tag{4}$$

$C_w = 0.15$, d_w is the wall distance, Δ_{nstep} is the grid step size in the wall-normal direction and Δ_{max} is according to Eq. 1. The intention of using Δ_{dw} is to get a smooth reduction of the turbulent viscosity close to the wall with a steep gradient in the off-wall region. This should be compared to a turbulent viscosity based on Δ_{vol}, which has a much steeper growth in the wall vicinity region with a slower growth in the outer part of the boundary layer.

The LES length scales in Eq. 1 to 4 are demonstrated in this paper in fully developed channel flow. Moreover, the RANS-LES interface is prescribed at four different locations from the wall for each LES length scale. The LES length scale based on the wall distance, i.e. Eq. 4, was shown to give the best results with respect to log-layer mismatch and was used in channel flow using embedded LES and the flow over a wall-mounted hump. The test cases used are further described in Section IV.

The paper is organized as follows. The PDH-LRN base model and the modifications in the proposed turbulence-resolving model are presented in Section II. The numerical method is presented in Section III. Results of the calibration and the evaluation of the different test cases using the proposed model are presented in Section IV. The work is summarized and concluded in Section V.

II. Model Formulation

II.A. Base Model

The LRN-PDH model is an improved variant of Wilcox's low-Reynolds-number model.[11] In the PDH-LRN model, an additional turbulent cross-diffusional term is added in the ω equation. Different from Menter's BSL and SST models,[12] the cross-diffusion term in PDH-LRN is active in the near-wall region. Close to the wall, the derivatives of k and ω are often of opposite signs, giving that the cross-diffusion term often acts as a sink term. In the near-wall region, k is thus increased due to the reduction of ω and, in turn, an increased turbulent viscosity is achieved. The model constants are recalibrated compared to Wilcox's LRN model and the near-wall damping functions are reconstructed. The transport equations and the turbulent viscosity for the PDH-LRN $k-\omega$ model are summarized.

$$\frac{D\rho k}{Dt} = \tau_{ij}\frac{\partial u_i}{\partial x_j} - D^k + \frac{\partial}{\partial x_j}\left[\left(\mu + \frac{\mu_t}{\sigma_k}\right)\frac{\partial k}{\partial x_j}\right] \tag{5}$$

$$\begin{aligned}\frac{D\rho\omega}{Dt} &= C_{\omega_1} f_\omega \frac{\omega}{k}\tau_{ij}\frac{\partial u_i}{\partial x_j} - C_{\omega 2}\rho\omega^2 \\ &+ \frac{\partial}{\partial x_j}\left[\left(\mu + \frac{\mu_t}{\sigma_\omega}\right)\frac{\partial \omega}{\partial x_j}\right] + C_\omega \frac{\mu_t}{k}\frac{\partial k}{\partial x_j}\frac{\partial \omega}{\partial x_j}\end{aligned} \tag{6}$$

$$\mu_t = C_\mu f_\mu \frac{\rho k}{\omega} \tag{7}$$

D/Dt on the left hand side of the transport equations is the material derivative; $D/Dt = \partial/\partial t + u_i \partial/\partial x_i$. The formulation of the wall boundary condition for ω reads:

$$\omega = \frac{6\nu}{C_{\omega 2} y^2} \tag{8}$$

As a further adaption to complex internal flows, the only governing parameter used in the damping functions, f_k, f_ω and f_μ, is the turbulent Reynolds number, Eq. 12. Compared to any wall distance related quantity, which can be an ambiguous quantity for complex internal flows, the turbulent Reynolds number is

well defined since no geometrical properties are involved. On the other hand, in a LES and hybrid RANS-LES perspective, the wall distance has been shown to be a suitable parameter to include in the formulation of the LES length scale.[10] Thus, in turbulence resolving simulations, it might be necessary to include the wall distance.

$$f_k = 1 - 0.722 \cdot \exp\left[-\left(\frac{R_t}{10}\right)^4\right] \tag{9}$$

$$f_\omega = 1 + 4.3 \cdot \exp\left[-\left(\frac{R_t}{1.5}\right)^{1/2}\right] \tag{10}$$

$$\begin{aligned} f_\mu = 0.025 \quad &+ \quad \left\{1 - \exp\left[-\left(\frac{R_t}{10}\right)^{3/4}\right]\right\} \\ &\times \quad \left\{0.975 + \frac{0.001}{R_t} \cdot \exp\left[-\left(\frac{R_t}{200}\right)^2\right]\right\} \end{aligned} \tag{11}$$

The turbulent Reynolds number is defined as:

$$R_t = \frac{k}{\nu\omega} \tag{12}$$

Finally, the closure constants for the PDH-LRN model are presented.

$$\sigma_k = 0.8 \quad \sigma_w = 1.35 \quad C_\mu = 1.0 \quad C_k = 0.09 \tag{13}$$

$$C_{\omega 1} = 0.42 \quad C_{\omega 2} = 0.075 \quad C_\omega = 0.75 \tag{14}$$

II.B. Formulation of the Turbulence-Resolving Mode

The turbulence-resolving mode in the proposed model is incorporated through the dissipation term in the k equation, which is modified in accordance with Strelets' SST-DES.[13]

$$D^k = C_k f_k \rho k \omega = \rho f_k \frac{k^{3/2}}{l_{turb}} \tag{15}$$

The turbulent length scale, expressed in terms of k and ω, is substituted in the dissipation term, which gives the possibility to formulate the hybrid RANS-LES model. The same expression is kept for the turbulent viscosity as in the base model formulation. However, the turbulent properties, k and ω, are either RANS or SGS properties depending on whether the model is used in RANS or LES mode. The turbulent length scale is chosen according to the modeling mode, i.e. $l_{turb} = l_{RANS}$ or $l_{turb} = l_{LES}$.

$$l_{RANS} = \frac{k^{1/2}}{C_k \omega} \tag{16}$$

$$l_{LES} = \Psi_{PDH} C_{LES} \Delta \tag{17}$$

With $l_{turb} = l_{RANS}$, the original PDH-LRN model is returned. When $l_{turb} = \Psi_{PDH} C_{LES} \Delta$, the LES mode of the proposed hybrid RANS-LES model is achieved. Δ is the LES length scale and $C_{LES} = 0.70$ was calibrated using decaying homogeneous isotropic turbulence (DHIT). These results are presented in more detail in Section IV. Since the PDH-LRN model uses low-Reynolds-number damping functions, the correction function, Ψ_{PDH}, is added to the LES formulation as recommended by Spalart et al.[9] Modeling constants and damping functions in the proposed model are according to the PDH-LRN model.[1]

Contrary to RANS models, where all turbulence is modeled, only the subgrid scale turbulence is modeled in LES. Thus, the local turbulent Reynolds numbers reach much lower levels as compared to RANS, which can activate the damping functions even though the flow is detached and when walls are far away. Since the amount of modeled turbulence is dependent of the grid resolution, the local turbulent Reynolds number and the turbulent viscosity are dependent of the grid resolution as well. Moreover, the amount of damping

achieved by the damping functions is hence dependent on the grid resolution, a dependency that has to be avoided. The purpose of the correction function, Ψ_{PDH}, is thus to eliminate the low-Reynolds-number damping made by the damping functions in the off-wall LES region and keep them in the RANS region. At local equilibrium, the introduction of Ψ_{PDH} is equal to de-activating the damping functions in LES mode. However, the damping functions should be used when RANS is applied. Through the introduction of the correction function in the LES length scale, the same set of model constants/equations can thus be used in the whole flow domain. The correction function will now be derived for the PDH-LRN model in accordance with the work of Mockett.[14]

A generalized form of the Smagorinsky turbulent viscosity can be formulated in a PDH-LRN framework using the function A_{PDH} and the correction function Ψ_{PDH}.

$$\nu_t = A_{PDH} \left(\Psi_{PDH} C_{LES} \Delta\right)^2 S \tag{18}$$

To return the original formulation of the Smagorinsky turbulent viscosity, the correction function should cancel the low-Reynolds-number dependency of A_{PDH} (A_{PDH} include the low-Reynolds-number damping functions), i.e. $A_{PDH}\Psi_{PDH}^2 = const.$ Assume that the proposed model is in LES mode (away from the wall) and that the turbulent transport equations are in local equilibrium, i.e. when production and dissipation/destruction balance in the k and ω equations. Note that, in a RANS framework, the k and ω equations cannot be in local equilibrium simultaneously. However, due to the introduction of the turbulence resolving mode through the dissipation term in the k equation, an extra degree of freedom is given to the turbulent transport equations, and local equilibrium can be simultaneously fulfilled away from the wall, see further Ref.[15] The k and ω equations in LES mode at local equilibrium are expressed.

$$\nu_t S^2 = f_k \frac{k^{3/2}}{\Psi_{PDH} C_{LES} \Delta} \tag{19}$$

$$\nu_t S^2 = \frac{C_{\omega 2}}{C_{\omega 1}} \frac{1}{f_\omega} \omega k \tag{20}$$

The turbulent viscosity, as expressed in Eq. 7, can be used to get an expression for the specific dissipation rate.

$$\nu_t = C_\mu f_\mu \frac{k}{\omega} \qquad \Longrightarrow \qquad \omega = C_\mu f_\mu \frac{k}{\nu_t} \tag{21}$$

The subgrid scale turbulent kinetic energy can be expressed by combining Eq. 20 and 21.

$$k = \sqrt{\frac{C_{\omega 1}}{C_{\omega 2}} \frac{f_\omega}{C_\mu f_\mu}} \nu_t S \tag{22}$$

Putting Eq. 22 in 19 forms an expression for the PDH-LRN Smagorinsky-like turbulent viscosity.

$$\nu_t = \frac{1}{f_k^2} \left(\frac{C_{\omega 2}}{C_{\omega 1}} \frac{C_\mu f_\mu}{f_\omega} \right)^{3/2} \left(\Psi_{PDH} C_{LES} \Delta\right)^2 S \tag{23}$$

Equations 18 and 23 give the expression for the function A_{PDH}.

$$A_{PDH} = \frac{1}{f_k^2} \left(\frac{C_{\omega 2}}{C_{\omega 1}} \frac{C_\mu f_\mu}{f_\omega} \right)^{3/2} \tag{24}$$

As seen, A_{PDH} depends on the damping functions, which in turn are functions of the local turbulent Reynolds number. To achieve $A_{PDH}\Psi_{PDH}^2 = const$, A_{PDH}^* is introduced in order to represent A_{PDH} when $R_t \to \infty$.

$$R_t \to \infty \Longrightarrow f_k,\ f_\omega,\ f_\mu \to 1 \tag{25}$$

$$A_{PDH}^* = \left(\frac{C_{\omega 2} C_\mu}{C_{\omega 1}} \right)^{3/2} \tag{26}$$

In correspondence with A_{PDH}^*, we seek a function $\Psi_{PDH}^* = 1$, i.e. Ψ_{PDH} when $R_t \to \infty$. The formulation of the correction function, including numerical limiters, can now be outlined.

$$\left(\frac{\Psi}{\Psi^*}\right)^2 = \frac{A^*}{A} \quad \Longrightarrow \quad \Psi_{PDH} = \min\left[10, f_k\left(\frac{f_\omega}{f_\mu}\right)^{3/4}\right] \tag{27}$$

The upper limit of Ψ is chosen according to Spalart et al.[9] The damping functions and the derived correction function are plotted in Figure 1 as a function of the turbulent Reynolds number.

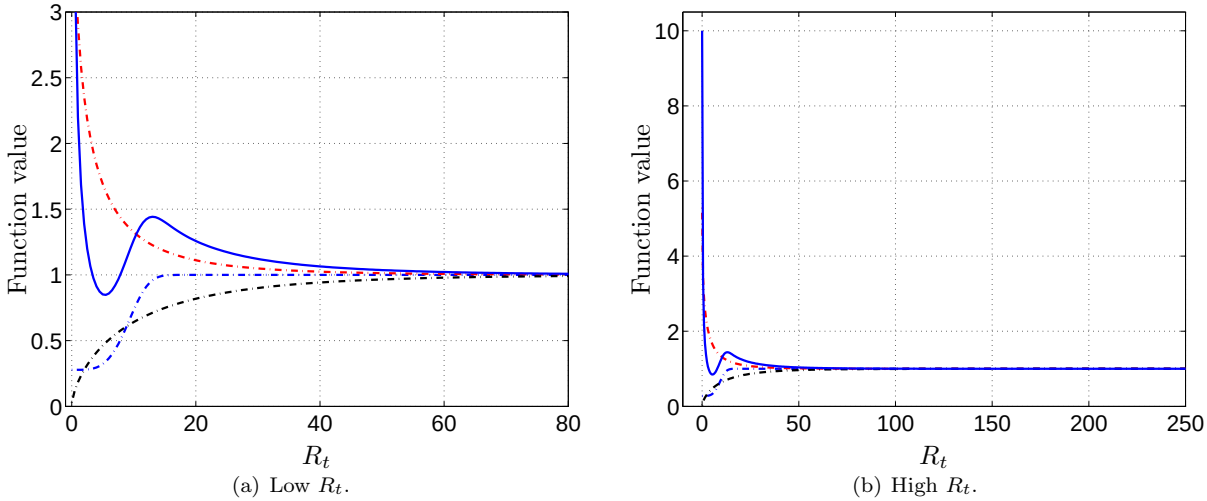

(a) Low R_t. (b) High R_t.

Figure 1. Damping functions and correction function used in the hybrid RANS-LES model based on PDH-LRN. - - - : f_k; -·- : f_ω; - - - : f_μ; ——— : Ψ_{PDH}.

II.C. Interface Formulations

Two different interface formulations have been used in the test cases where an embedded LES approach has been applied. In the channel flow case, the RANS and LES domains are coupled and solved simultaneously. In the hump flow case, a precursor RANS computation using Menter's SST $k-\omega$ model[12] (MSST) has been used to establish the turbulent properties (k and ω) on the RANS-LES interface for the subsequent zonal RANS-LES simulation downstream of the interface. To stimulate the development of turbulence resolving flow, anisotropic turbulent velocity fluctuations from synthetic turbulence[16] were added to the mean flow field at the interface as additional source terms in the continuity and momentum equations in both cases.

For the channel flow using embedded LES, the RMS values of the imposed synthetic normal stresses are constant across the channel height. The imposed synthetic shear stress ($\langle u'v' \rangle$) was set constant across the channel height, but with a change of sign at the channel center line. For the hump flow, the added turbulent velocity fluctuations are scaled with the RANS turbulent kinetic energy profile at the interface. The imposed turbulent fluctuations at the interfaces are shown in Figure 2 and 3.

Moreover, the convective and diffusive fluxes of k and ω were modified across the interface to match typical SGS levels and to speed up the growth of resolved turbulence. The subgrid scale turbulent kinetic energy at the interface in channel flow of embedded LES was estimated from Eq. 28, where $0.025 < f_{k,int} < 0.20$ was investigated. The specific interface SGS dissipation rate is computed according to Eq. 29.

$$k_{sgs,int} = f_{k,int} \cdot k_{RANS} \tag{28}$$

$$\omega_{sgs,int} = \frac{k_{sgs,int}^{1/2}}{C_k \cdot \Psi_{PDH} C_{LES} \Delta} \tag{29}$$

For the hump flow case, where the upstream RANS domain and the downstream zonal RANS-LES simulations are not solved simultaneously, Eq. 29 cannot be used since Ψ_{PDH} is dependent on the local turbulent Reynolds number, which in turn is a function of ω. The specific dissipation rate in the LES region on the interface is therefore computed using Eq. 30 to 32.

$$\epsilon_{sgs} = \epsilon_{RANS} \tag{30}$$

$$\epsilon_{sgs} = C_k \left(k\omega\right)_{sgs} \tag{31}$$

$$\omega_{sgs,int} = \frac{\epsilon_{sgs}}{C_k k_{sgs}} = \frac{\epsilon_{sgs}}{C_k f_{k,int} k_{RANS}} \tag{32}$$

The specific dissipation rate in the RANS region, i.e. in the near-wall region of the zonal RANS-LES simulation, is taken from the precursor RANS computation.

The SGS turbulent kinetic energy at the interface is also computed using Eq. 28 for the hump flow. The interval $0.05 \leq f_{k,int} \leq 0.20$ was investigated. In the RANS region, $f_{k,int} = 1$. However, only minor changes in the flow downstream of the interface have been observed for different values of $f_{k,int}$. Therefore, for the hump flow case in Section IV, only results from simulations using $f_{k,int} = 0.10$ are presented.

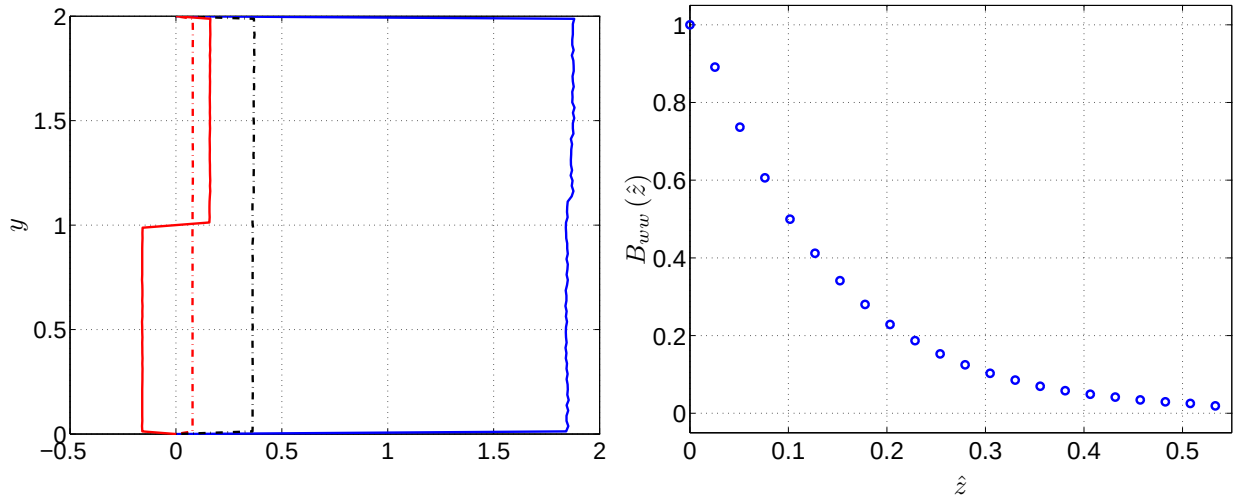

(a) ——: u^2_{rms}/u^2_τ; -·-·: v^2_{rms}/u^2_τ; - - -: w^2_{rms}/u^2_τ; ——: $\langle u'v' \rangle / u^2_\tau$. (b) Two-point correlation.

Figure 2. Channel flow using embedded LES. Prescribed synthetic Reynolds stresses at the interface.

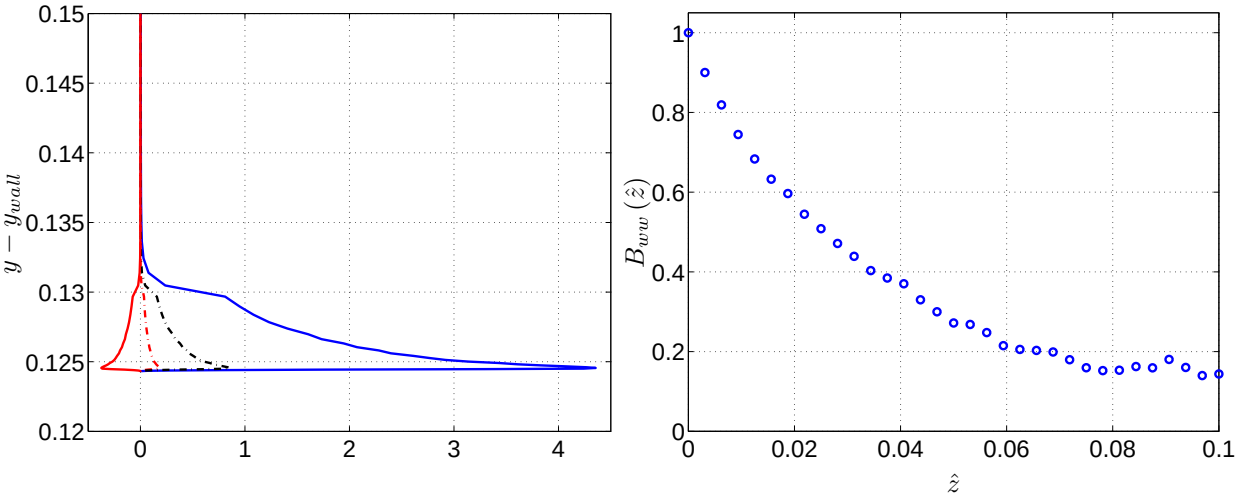

(a) ——: u^2_{rms}/u^2_τ; -·-·: v^2_{rms}/u^2_τ; - - -: w^2_{rms}/u^2_τ; ——: $\langle u'v' \rangle / u^2_\tau$. (b) Two-point correlation.

Figure 3. Hump flow using embedded LES. Prescribed synthetic Reynolds stresses at the interface.

III. Numerical Method

Since zonal and embedded formulations of the proposed model are examined, both unsteady RANS and LES are applied in the same domain. The modeling mode, i.e. RANS or LES, determines whether the Navier-Stokes equations are either time averaged or spatially filtered. The incompressible solver used in this work is based on a finite volume technique; the spatial filter width is therefore constituted by the local cell size, Δ. In the following equations, the bar ($\overline{\cdot}$) indicates time averaging or spatial filtering of a quantity. Since heat transfer was not of interest in the flow problems analyzed, constant density was applied in all simulations. The continuity and momentum equations, where time averaging or spatial filtering were applied, read

$$\frac{\partial \overline{u}_i}{\partial x_i} = 0 \tag{33}$$

$$\frac{\partial \overline{u}_i}{\partial t} + \frac{\partial \left(\overline{u}_i \overline{u}_j\right)}{\partial x_j} = -\frac{1}{\rho}\frac{\partial \overline{p}}{\partial x_i} + \frac{\partial}{\partial x_j}\left[\left(\nu + \nu_t\right)\frac{\partial \overline{u}_i}{\partial x_j}\right] \tag{34}$$

where ν_t denotes the turbulent viscosity, which need to be modeled. Due to the different modeling modes, the turbulent viscosity is either a RANS or a subgrid scale property.

In the simulations of fully developed channel flow, the term $\beta\delta_{1i}$, representing the driving pressure gradient ($\beta = 1$), is added on the right hand side of the momentum equations in order to balance the channel wall shear stress.

The solver used offers different spatial discretization schemes: central differencing, van Leer and a hybrid scheme. Different schemes were applied depending on the application and are specified in the next section. The temporal advancement is made with a second order Crank-Nicolson scheme. An implicit, fractional step technique with a multigrid Poisson solver[17] was used on a non-staggered grid arrangement. For a more detailed description of the numerical procedure, see Davidson and Peng.[6]

IV. Calibration and Evaluation

In a first step to evaluate the PDH-LRN as a base model for turbulence resolving simulations, four test cases were analyzed; Decaying Homogeneous Isotropic Turbulence (DHIT), fully developed channel flow, channel flow using embedded LES and flow over a wall mounted hump. In fully developed channel flow and in channel flow using embedded LES, the proposed model was evaluated for $Re_\tau = 8000$ and $Re_\tau = 950$, respectively. The wall-modeled LES (WMLES) capability, where the near-wall RANS region acts as the wall model, is evaluated in the channel flow computations at $Re_\tau = 8000$. The capability of the proposed interface condition used in embedded LES is evaluated in the channel flow (embedded LES) as well as in the hump flow case. Further, the modeling capability of predicting flow separation on a smoothly curved surface is examined in the hump flow, as well as in the prediction of large scale flow separation.

IV.A. Decaying Homogeneous Isotropic Turbulence

The turbulence resolving mode and the constant C_{LES} of the proposed hybrid RANS-LES model were calibrated using Decaying Homogeneous Isotropic Turbulence (DHIT). Experimental benchmark data by Comte-Bellot and Corrsin[18] were used in this work for comparison.

DHIT was computed on two grids to investigate the effect of grid density on C_{LES}. Each grid, with a domain size of $(2\pi)^3$, consisted of 32^3 and 64^3 cubic shaped cells, respectively. For each grid, the test case was computed both with and without the activation of the correction function, Ψ_{PDH}. A simulation was also made on the 64^3 grid, where the correction function was excluded and the damping functions were set to 1 to verify a correct behaviour of Ψ_{PDH}. Periodic boundary conditions were applied in all directions, and the simulation was initiated with a prescribed velocity field with zero mean velocity. To reach adequate start values for k and ω, 4000 iterations were computed with a frozen velocity field, which was used as an initial condition for the unsteady DHIT simulation. The simulations were performed using a second order central differencing scheme for the continuity and momentum equations and a first order hybrid scheme for the k and ω transport equations. The initial velocity fields were generated by a widely used computer program from the group of Professor Strelets in St. Petersburg. Spectra are presented at two non-dimensional time steps: $T = 0.87$ and 2.0.

The criteria used to select the best suited C_{LES}-value are according to Bunge.[19] In short, this means that the 32^3 grid is given priority over the 64^3 grid. The 32^3 grid is seen as more representative for grids used in practical hybrid RANS-LES simulations of complex geometries/flows. Furthermore, $T = 2$ has precedence over $T = 0.87$.

Energy spectra from DHIT simulations using the proposed model are presented in Figures 4 and 5.

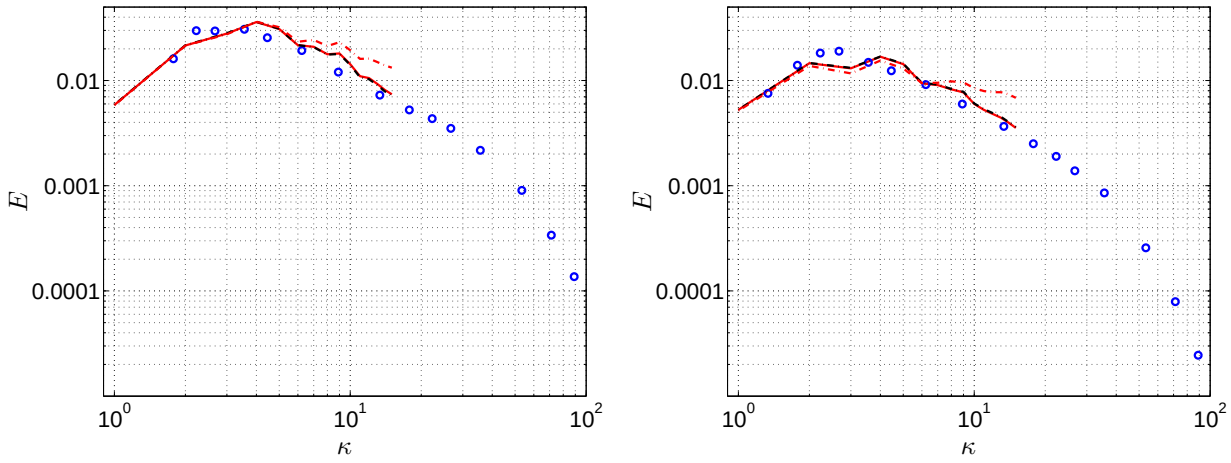

(a) $T = 0.87$ (b) $T = 2$

Figure 4. Energy spectra from DHIT using PDH-LRN on a 32^3 cell grid. ——— **: Ψ_{PDH} active ($C_{LES} = 0.70$);** - · - · **: $\Psi_{PDH} = 1$ ($C_{LES} = 0.70$);** - - - **: $\Psi_{PDH} = 1$ ($C_{LES} = 0.95$).** ○**: Experiments.**[18]

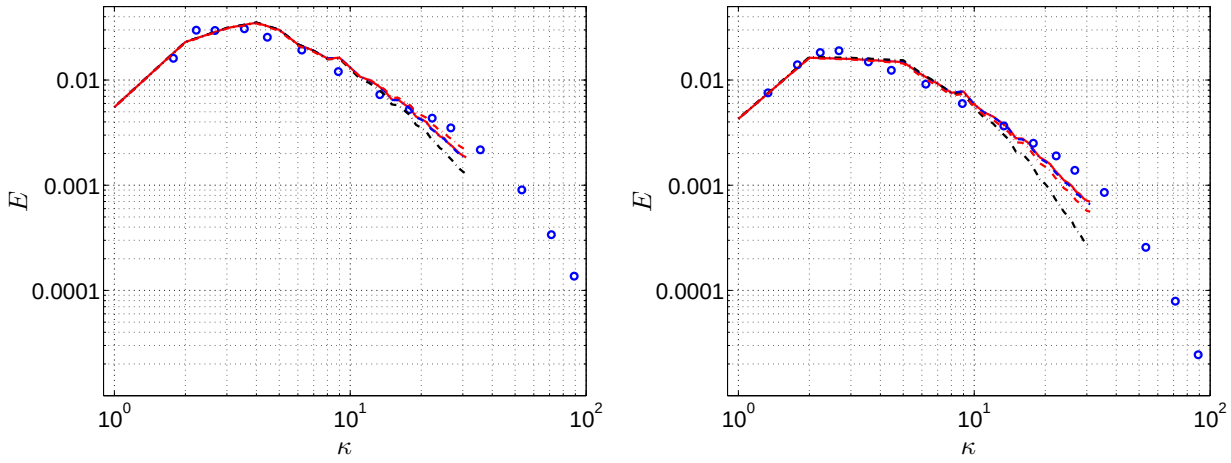

(a) $T = 0.87$ (b) $T = 2$

Figure 5. Energy spectra from DHIT using PDH-LRN on a 64^3 cell grid. ——— **: Ψ active ($C_{LES} = 0.70$);** - · - · **: $\Psi_{PDH} = 1$ ($C_{LES} = 0.70$);** - - - **: $\Psi_{PDH} = 1$ ($C_{LES} = 0.95$);** - · · - **: $\Psi_{PDH} = 1$ and $f_k = f_\omega = f_\mu = 1$ ($C_{LES} = 0.70$).** ○**: Experiments.**[18]

On the coarse grid, the proposed model was calibrated with and without the correction function, giving $C_{LES} = 0.70$ and 0.95, respectively. As seen in Figure 4, the results are identical. Using $C_{LES} = 0.70$, but without the correction function, the decay of turbulence is too weak on the 32^3 grid. Compared to the simulations on the finer 64^3 grid shown in Figure 5, $C_{LES} = 0.95$ gives too strong a decay as compared to experimental data. Comparing the two simulations on the fine grid where the correction function and the damping functions were set to 1 and the other where Ψ_{PDH} was active and $C_{LES} = 0.70$, an identical decay of turbulence is achieved, which shows an adequate behaviour of the correction function. For higher wave numbers (κ), as observed on the finer grid, the decay is slightly overpredicted, even though the correction function is activated.

The simulations presented in Figures 4 and 5, show, according to the selection criteria, that $C_{LES} = 0.70$

is a representative value for the proposed model and is in line with other well known base RANS models used for hybrid RANS-LES modeling.

In engineering applications, a grid density corresponding to the coarse grid is often more representative than the finer grid. The stronger influence of Ψ_{PDH} seen on the coarse grid thus motivates its use, even though the influence of the low Reynolds number correction function is weak on the 64^3 grid.

IV.B. Fully Developed Channel Flow Using Zonal RANS-LES, $Re_\tau = 8000$

The Reynolds number based on friction velocity u_τ and half channel height δ is for this flow $Re_\tau = 8000$. The grid used in the simulations is presented in Table 1.

Table 1. Grid used in fully developed channel flow.

Re_τ	$(x/\delta, y/\delta, z/\delta)$	(n_x, n_y, n_z)	$(\Delta x^+, \Delta y^+, \Delta z^+)$
8000	$(3.2, 2, 1.6)$	$(64, 96, 64)$	$(400, 1.7 - 1050, 200)$

Periodic boundary conditions are applied in the streamwise and spanwise directions. In addition, a driving pressure gradient is applied in the streamwise direction to achieve fully developed channel flow. No-slip conditions are applied on the bottom and top walls. For the continuity and momentum equations a second order central differencing scheme was applied, and for the turbulent transport equations a first order hybrid scheme was used. Due to the prescribed driving pressure gradient in the streamwise direction, the mass flow rate is not pre-defined but is rather model dependent. The test case aims at hybrid RANS-LES modeling and a zonal formulation with prescribed RANS-LES switch locations, see Figure 6.

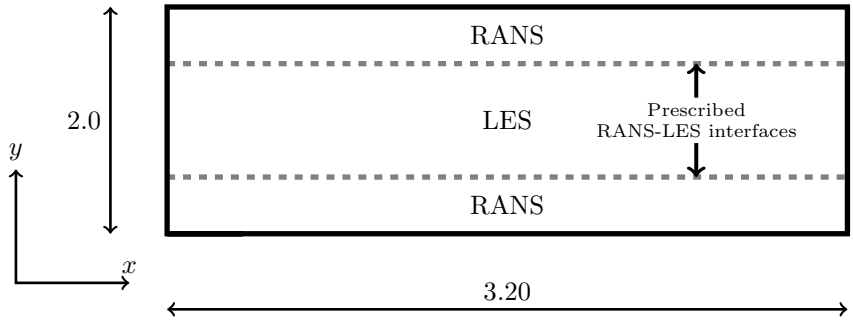

Figure 6. Channel flow configuration for zonal RANS-LES.

A zonal formulation was chosen in order to evaluate the influence of switch location on the behavior of the model and how the different LES length scale formulations affect the log-layer mismatch, which is a common problem in hybrid RANS-LES simulations of attached boundary layer flows. The four prescribed locations were chosen so that the transition from RANS to LES occurred at $y^+ = 120$, $y^+ = 250$, $y^+ = 520$ and $y^+ = 1050$. With these four locations, Δ_{max}, Δ_{vol}, Δ_Ω and Δ_{dw} were evaluated, see further Eq. 1 to 4. The turbulent length scales, using different definitions of Δ and the RANS-LES switch at $y^+ = 250$ are shown in Figure 7.

For $y^+ \leq 250$, $l_{turb} = l_{RANS}$, and for $y^+ > 250$, $l_{turb} = l_{LES}$, according to Eq. 16 and 17. The major reason for the decrease in l_{turb}/Δ_{max} for $y^+ > 2800$, especially for Δ_Ω and Δ_{vol}, is due to the grid design. For $y^+ < 2800$, the local maximum cell size is constant and equal to Δ_x. For larger y^+-values, $\Delta_{max} = \Delta_y$, which increases away from the wall until the centerline is reached. The effect of Ψ_{PDH} also contributes since the local turbulent Reynolds number decreases in the center part of the channel.

The measure of skin-friction reduction was used to quantify the log-layer mismatch as in Nikitin et al.[20] Instead of extrapolating DNS data, as in Nikitin et al.,[20] the log-law was used to compute the center line velocity and the skin friction coefficient as in Eq. 35.

$$U^+_{cl,th} = \frac{\log(Re_\tau)}{\kappa} + 5.2 \quad \Longrightarrow \quad C_{f,th} = \frac{2}{\left(U^+_{cl,th}\right)^2} \tag{35}$$

Where $Re_\tau = 8000$ and $\kappa = 0.41$. The skin friction reduction was computed as; $\Delta C_f = (C_f - C_{f,th})/C_{f,th}$, where $C_{f,th}$ refers to the theoretical skin friction calculated from $U^+_{cl,th}$ and C_f is the skin friction coefficient

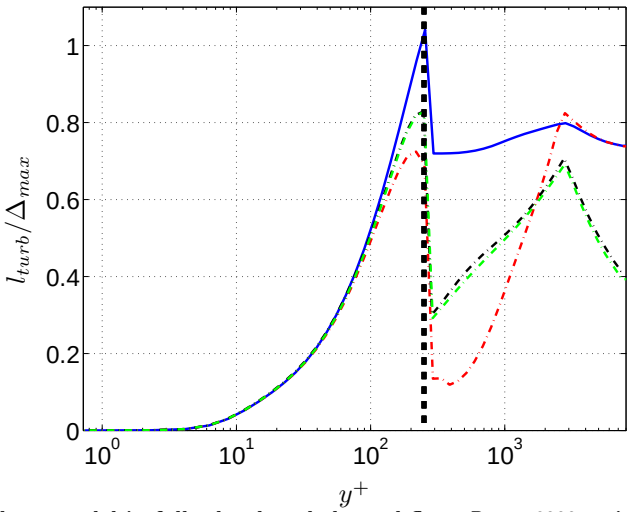

Figure 7. PDH-LRN as the base model in fully developed channel flow, $Re_\tau = 8000$, using different LES length scales. RANS-LES interface at $y^+ = 250$. ——: $\Delta = \Delta_{max}$; -·-·-: $\Delta = \Delta_{dw}$; - - -: $\Delta = \Delta_\Omega$; -·-·-: $\Delta = \Delta_{vol}$. Interface location indicated by dashed black line.

computed from the simulations presented.

Due to the wide use of Menter's $k-\omega$ SST model as a base model in aerodynamic hybrid RANS-LES applications, it was used for comparison with the model proposed in this work. However, the aim of this comparison is not to evaluate whether PDH-LRN or MSST is best suited as a base RANS model for hybrid RANS-LES modeling. Instead, MSST is used to show that the hybrid RANS-LES formulation based on PDH-LRN has correct RANS-LES switch characteristics and that the proposed subgrid scale model works as expected. Comparative simulations using the PDH-LRN and MSST base models are shown in Figure 8. For these simulations, the RANS-LES switch was prescribed at $y^+ = 520$, and the LES length scales used were $\Delta = \Delta_{max}$ and Δ_{dw}.

In Figure 8 (a), it is observed that the effect of the RANS-LES interface is less distinct using the MSST as a base model compared to the PDH-LRN model. A more abrupt increase in velocity is observed with the PDH-LRN model. However, the centerline velocities are in better agreement with the log-law for both LES length scales in PDH-LRN compared to MSST. Moreover, using the MSST base model, the LES region has a stronger influence on the near-wall RANS region, which can be explained by the lower level of turbulent viscosity produced by the MSST RANS model, see Figure 8 (b). The lower turbulent viscosity in the RANS-LES interface region is also reflected in the higher level of resolved shear stress, using the MSST compared to PDH-LRN, as shown in Figure 8 (c). The underprediction of skin friction due to the log-layer mismatch for the MSST and PDH-LRN simulations is presented in Table 2 and 3.

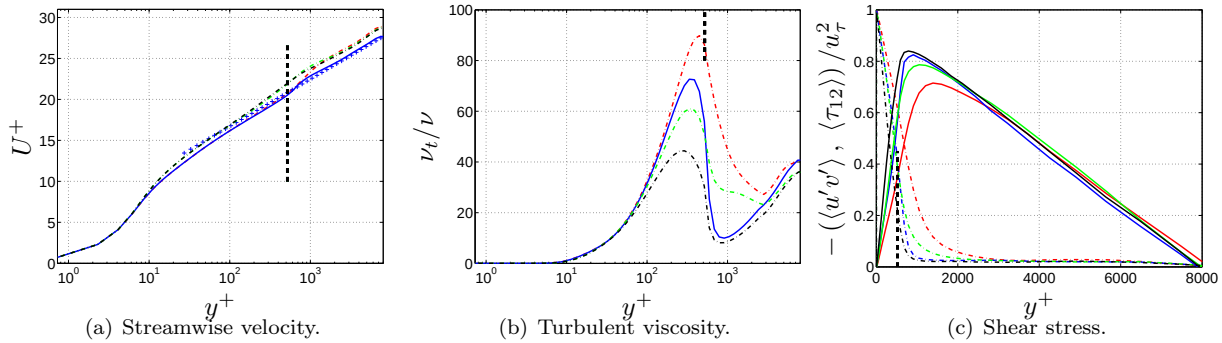

(a) Streamwise velocity. (b) Turbulent viscosity. (c) Shear stress.

Figure 8. Fully developed channel flow, $Re_\tau = 8000$. Comparison of PDH-LRN and MSST as base models. Interface at $y^+ = 520$. ——: PDH-LRN, $\Delta = \Delta_{dw}$; -·-·-: PDH-LRN, $\Delta = \Delta_{max}$; - - -: MSST, $\Delta = \Delta_{dw}$; -·-·-: MSST, $\Delta = \Delta_{max}$. Interface location indicated by dashed black line. (a) Streamwise time-averaged velocity. (b) Turbulent viscosity. (c) Resolved (solid lines) and modeled+viscous (dash-dotted lines) shear stress.

The overall behavior of the hybrid RANS-LES formulation based on PDH-LRN is comparable with MSST. Both subgrid scale models perform well, and most of the differences observed in the results can be related

to the RANS zone, where clear differences are present between the models.

From this brief analysis, made to justify a reasonable behavior of PDH-LRN as a base model, a more thorough analysis of the simulations performed with the proposed model will now be presented.

The abrupt increase in velocity in the log-law region seen in Figure 9 indicates a log-layer mismatch. Figure 9 (a) shows different locations at which the model switches from RANS to LES using Δ_{max}. Comparing the computed skin friction reduction for Δ_{max}, presented in Table 2, it is observed that the log-layer mismatch is increased when the switch is moved closer to the wall. Analyzing Figure 9 (b), where different interface locations are compared for Δ_{dw}, together with Table 2, it is seen that the best predicted velocity profile is given for the RANS-LES switch at $y^+ = 250$, while the over prediction is enhanced for the switch locations at $y^+ = 120$, $y^+ = 520$ and 1050. At $y^+ = 1050$, the LES length scales based on the local maximum size and the wall distance, give velocity profiles comparable to each other.

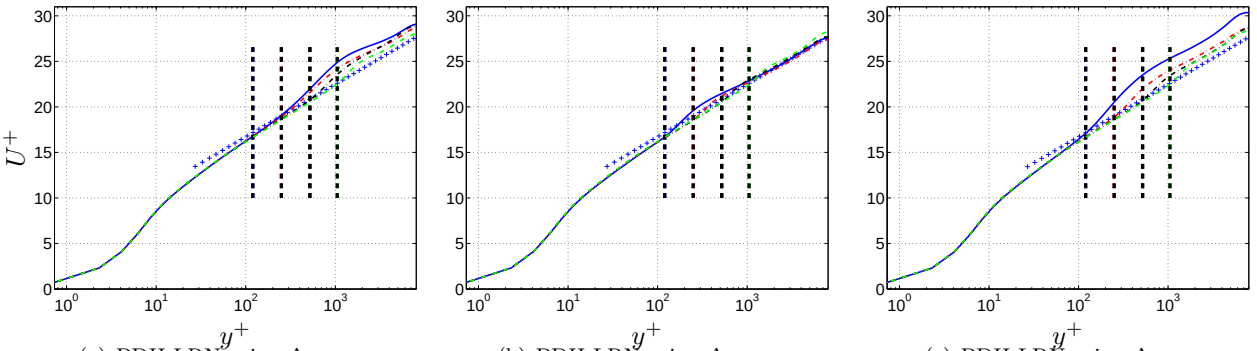

(a) PDH-LRN using Δ_{max}. (b) PDH-LRN using Δ_{dw}. (c) PDH-LRN using Δ_{Ω}.

Figure 9. Fully developed channel flow, $Re_\tau = 8000$, using PDH-LRN with different RANS-LES switch locations. Streamwise time-averaged velocity. ——: $y^+ = 120$; - - -: $y^+ = 250$; - - -: $y^+ = 520$; - - -: $y^+ = 1050$. Switch locations indicated by black dashed lines. (a) Δ_{max}. (b) Δ_{dw}. (c) Δ_{Ω}.

Figure 9 (c) presents velocity profiles for Δ_{Ω}. Overall, the vorticity based LES length scale gives the strongest log-layer mismatch on the grid used. The formulation based on the cube root of the local control volume gives results very similar to Δ_{Ω} on the grid used and is therefore only included in Table 3. For a more thorough comparison, see the work of Arvidson.[15] Even though the velocity profiles in some of the cases presented are substantially overpredicted in the LES region using the proposed model, the results are in agreement with the simulations presented by Nikitin et al.[20] in their study of using DES as a WMLES approach.

Table 2. Simulations using Δ_{max} and Δ_{dw}.

Base model	Δ_{LES}	y^+_{switch}	ΔC_f
PDH-LRN	Δ_{max}	120	-15.6%
PDH-LRN	Δ_{max}	250	-13.7%
PDH-LRN	Δ_{max}	520	-8.4%
MSST	Δ_{max}	520	-11.2%
PDH-LRN	Δ_{max}	1050	-5.4%
PDH-LRN	Δ_{dw}	120	-3.1%
PDH-LRN	Δ_{dw}	250	-1.8%
PDH-LRN	Δ_{dw}	520	-4.0%
MSST	Δ_{dw}	520	-10.6%
PDH-LRN	Δ_{dw}	1050	-7.4%

Table 3. Simulations using Δ_{Ω} and Δ_{vol}.

Base model	Δ_{LES}	y^+_{switch}	ΔC_f
PDH-LRN	Δ_{Ω}	120	-20.2%
PDH-LRN	Δ_{Ω}	250	-10.3%
PDH-LRN	Δ_{Ω}	520	-10.3%
MSST	Δ_{Ω}	520	-13.0%
PDH-LRN	Δ_{Ω}	1050	-8.3%
PDH-LRN	Δ_{vol}	120	-19.5%
PDH-LRN	Δ_{vol}	250	-11.0%
PDH-LRN	Δ_{vol}	520	-8.6%
MSST	Δ_{vol}	520	-13.5%
PDH-LRN	Δ_{vol}	1050	-10.4%

The level of turbulent viscosity produced is essentially the core of the log-layer mismatch issue. Analyzing Figure 10, large differences are observed between the LES length scale formulations. For the RANS-LES switch at $y^+ = 1050$, the different LES length scale formulations have only a small effect on the maximum turbulent viscosity produced in the RANS zone. Larger differences are recognized in the interface and off-wall

flow regions.

The reduction of ν_t/ν for Δ_Ω at the interface are almost as fast as for Δ_{dw}, but the lowest level reached in the interface region is higher for all switch locations except $y^+ = 1050$, where the levels produced with Δ_{dw} and Δ_Ω are similar. With Δ_{max}, the slowest reduction of turbulent viscosity is observed at the interface. The highest levels of turbulent viscosity are also given with Δ_{max} in the RANS and LES regions compared to the other LES length scales. However, the levels reached at the center line are similar with Δ_{max} and Δ_{dw}, since the maximum local cell size is applied here with both length scale formulations (see Eq. 1 and 4).

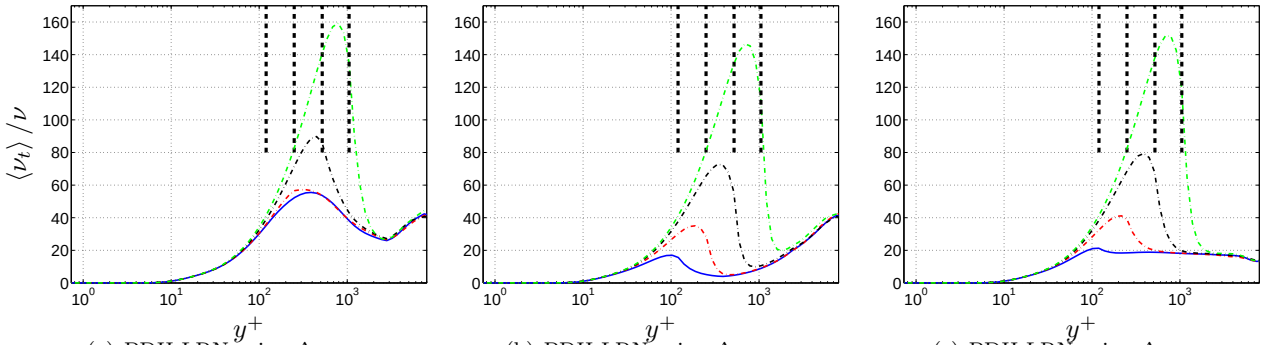

(a) PDH-LRN using Δ_{max}. (b) PDH-LRN using Δ_{dw}. (c) PDH-LRN using Δ_Ω.

Figure 10. Fully developed channel flow, $Re_\tau = 8000$, using PDH-LRN with different RANS-LES switch locations. Turbulent viscosity. ——: $y^+ = 120$; - - -: $y^+ = 250$; - · - ·: $y^+ = 520$; - · -: $y^+ = 1050$. Switch locations indicated by black dashed lines. (a) Δ_{max}. (b) Δ_{dw}. (c) Δ_Ω.

Figure 11 shows modeled and resolved shear stress. The rapid reduction in ν_t at the interface with Δ_{dw} is clearly reflected in the resolved shear stress levels seen in Figure 11 (b). The LES length scale based on Δ_{dw} gives the highest peak of resolved shear stress of all four length scales. With the interface at $y^+ = 520$, the resolved shear stress already seen at the interface represents 55 percent of the total shear stress level with Δ_{dw}, which should be compared to 33 percent for Δ_{max}.

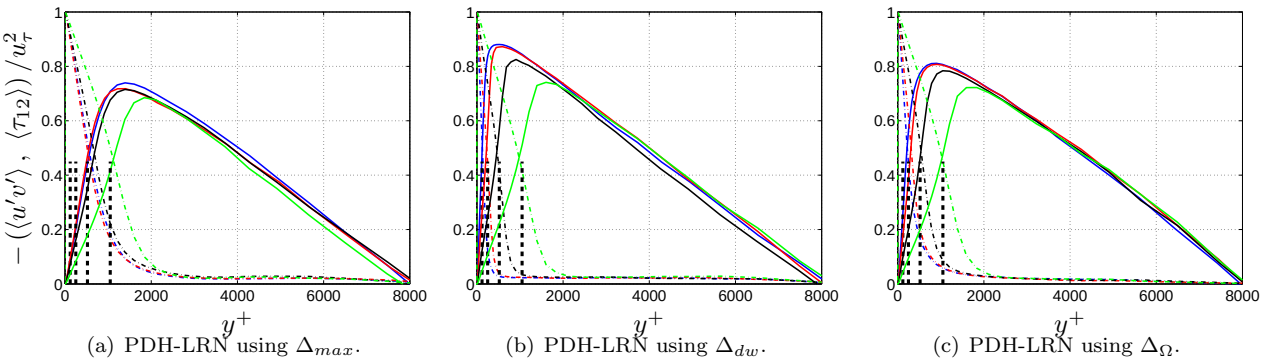

(a) PDH-LRN using Δ_{max}. (b) PDH-LRN using Δ_{dw}. (c) PDH-LRN using Δ_Ω.

Figure 11. Fully developed channel flow, $Re_\tau = 8000$, using PDH-LRN with different RANS-LES switch locations. Resolved (solid lines) and modeled+viscous (dash-dotted lines) shear stress. ——: $y^+ = 120$; ——: $y^+ = 250$; ——: $y^+ = 520$; ——: $y^+ = 1050$. Switch locations indicated by black dashed lines. (a) Δ_{max}. (b) Δ_{dw}. (c) Δ_Ω.

Even though the off-wall turbulent viscosity with Δ_Ω is smaller than that produced with Δ_{max} and Δ_{dw}, Figure 11 shows a negligible difference in the modeled stress levels in the off-wall region between different LES length scales. This is caused by the modeled stresses' dependency on the velocity gradients. Those are weak in the LES region around the center line, where the largest differences in turbulent viscosity are present, and thus small discrepancies are observed in the modeled stresses in this region compared to the interface region. Moreover, it can be concluded that the lower level of ν_t produced in the interface region with Δ_{dw}, compared to the other LES length scales analyzed, is the key issue in terms of generating an accurate turbulence resolving flow and reducing the log-layer mismatch.

For zonal RANS-LES computations of fully developed channel flow that are presented, the LES length scale based on Δ_{dw} shows a superiority to Δ_{max}, Δ_{vol} and Δ_Ω on the grid analyzed with regard to a reduction of the log-layer mismatch, especially when a large part of the boundary layer is simulated with LES. Compared to the LES length scale based on the wall-distance, the vorticity based length scale produces

a lower turbulent viscosity in the off-wall region, which is preferable for cases in which free shear flows are present for reducing the grey area zone.

IV.C. Channel Flow Using Embedded LES

As a first step towards more advanced flow cases, relying on an embedded approach, channel flow using embedded LES is explored with the proposed hybrid RANS-LES model. The purpose of the test case is to evaluate the use of the correction function in an embedded LES approach as well as other interface parameters. For complex internal flows, such as inlets and nozzles on low-observable UAVs, an embedded approach is attractive. An upstream attached boundary layer can be modeled with RANS, and a subsequent separated flow can be treated with accurate turbulence-resolving methods. The number of computational grid points can be reduced with a methodology of this kind, which is important for industrial use, and the most suitable method can be applied in each flow region.

The grid used for the channel flow is described in Table 4. A velocity profile from a precursor RANS simulation of fully developed channel flow at $Re_\tau = 950$, using PDH-LRN, was applied as inlet boundary condition to the RANS region. Periodic boundary conditions were used in the spanwise direction, and a Neumann boundary condition was used for the outlet section.

Table 4. Grid used in channel flow of embedded LES.

Re_τ	$(x/\delta, y/\delta, z/\delta)$	(n_x, n_y, n_z)	$(\Delta x^+, \Delta y^+, \Delta z^+)$	x_{int}/δ
950	$(3.2, 2, 1.6)$	$(64, 82, 64)$	$(48, 0.60 - 103, 24)$	1

A RANS-LES interface plane was employed at $x/\delta = 1$, see Figure 12. The flow downstream of the interface was simulated using full LES with PDH-LRN as the base model, i.e. no RANS layer was applied in the near-wall region. For greater detail on using the PDH-LRN as the base model in full LES of fully developed channel flow, the reader is referred to the work of Arvidson.[15] The upstream RANS and downstream LES domains were coupled and computed simultaneously.

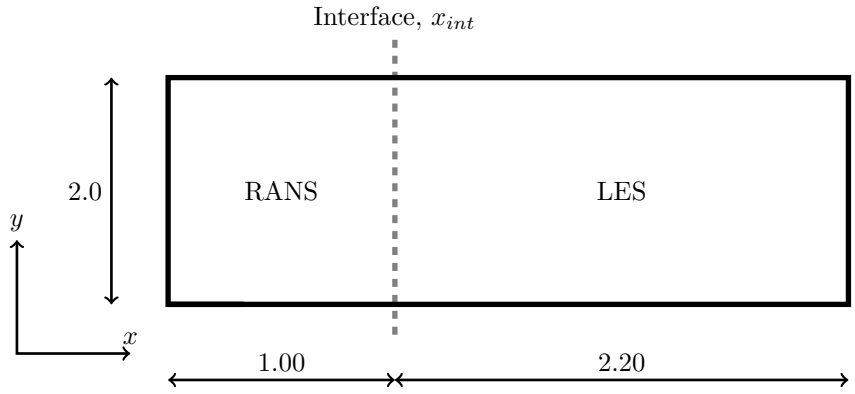

Figure 12. Channel flow configuration for embedded LES.

The RANS diffusion and convection fluxes across the interface in the k and ω equations were modified to reach typical SGS levels. From the simulations of fully developed channel flow, Δ_{dw} was concluded to be the best suited LES length scale for the proposed model. All simulations of channel flow using embedded LES presented are therefore made with $\Delta = \Delta_{dw}$.

Second order upwind (van Leer) and second order central differencing schemes were used for the continuity and momentum equations in the RANS and LES regions, respectively. The turbulent transport equations were discretized using a first order hybrid scheme. The same time step, $\Delta t = 1 \cdot 10^{-3}\ s$, was applied in both the RANS and LES domains in the simulations.

Simulations with $f_{k,int} = 0.050$ (see Eq. 28) have been evaluated for two different domain extensions in the streamwise direction, see Arvidson.[15] Only simulations on the shorter domain are presented in this paper since a negligible influence of the results between the two domains was observed using $f_{k,int} = 0.050$. Thus it was possible to make the evaluation of how $f_{k,int}$ influences the flow on the shorter domain. The interface parameters used in the simulations are described in Section II.

In fully developed channel flow, the mass flow rate is not prescribed since the flow is recirculated owing to the periodic boundary conditions in the streamwise direction. For a well converged solution of fully developed flow, the driving pressure gradient balances the wall shear stress. In contrast, in this channel flow case of embedded LES, the mass flow rate at the RANS-LES interface is prescribed from the upstream RANS domain. Thus the driving pressure gradient does not necessarily need to balance the wall shear stress, since the flow is not fully developed. This happens in the simulations presented here, since the LES model does not manage to re-create the RANS velocity profile, and the only way to compensate for these differences is through a change in the skin friction.

The turbulent viscosity in the proposed modeling approach is proportional to $f_{k,int}^{1/2}$, and the model shows a weak sensitivity to $f_{k,int}$. At $x/\delta = 3.025$, small differences are observed in the velocity profiles and the resolved stresses, as seen in Figures 13 and 14. The low values of turbulent viscosity given in the near-wall region almost disable the subgrid scale model, and thus the differences between different interface conditions are negligibly small in this region. Further out from the wall, the turbulent viscosity level increases and the subgrid scale model starts to play a more important role. Analyzing Figure 14 (b), it is recognized that the discrepancies in resolved normal stresses between the interface conditions are distinguishable for $y > 0.1$ ($y^+ > 100$). The high RMS values observed in the off-wall region are related to the synthetic fluctuations, which have a constant RMS value across the channel height. However, the slope of u^+_{rms} is better captured with higher $f_{k,int}$. Due to the higher $f_{k,int}$, a higher level of subgrid scale turbulent kinetic energy is prescribed at the interface, giving a higher level of turbulent viscosity, which in turn increases the damping effect of the velocity fluctuations. The difference in ν_t is also observed as a weak effect in the resolved shear stress presented in Figure 14 (a). As for the zonal RANS-LES simulations at $Re_\tau = 8000$, the large difference in ν_t in the outer boundary layer does not have a strong influence on the modeled stresses since the velocity gradients are small in this region.

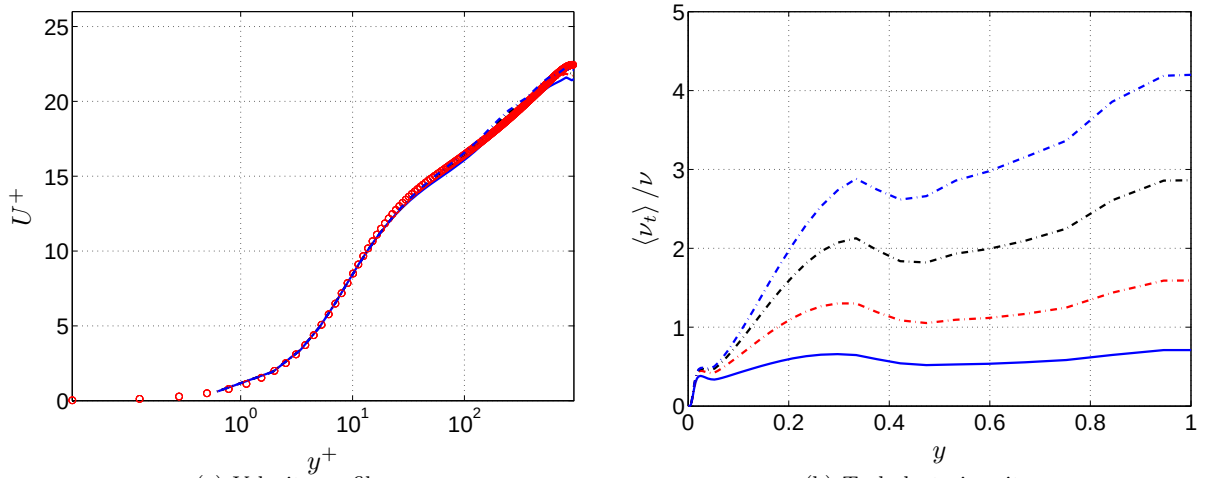

(a) Velocity profiles.

(b) Turbulent viscosity.

Figure 13. Channel flow using embedded LES. PDH-LRN with Δ_{dw}. Time-averaged streamwise velocity and turbulent viscosity at $x/\delta = 3.025$. ——: $f_{k,int} = 0.025$; - - -: $f_{k,int} = 0.050$; - - -: $f_{k,int} = 0.100$; - - -: $f_{k,int} = 0.200$. Markers are DNS data.[21]

The effect of the modified fluxes of the turbulent quantities over the interface is plotted in Figure 15 (a), where the streamwise peak level of the turbulent viscosity is presented. From the RANS level of $\nu_t/\nu = 115$, the turbulent viscosity is reduced to $\nu_t/\nu = 0.4 - 1.2$ for increased $f_{k,int}$ immediately downstream of the interface. An overshot in the turbulent viscosity is observed just upstream of the interface, reaching a value of $\nu_t/\nu = 170$ for $f_{k,int} = 0.025$. The peak is slightly increased for higher $f_{k,int}$ values. This is probably due to the synthetic turbulence applied at the interface, which generates resolved turbulence upstream of the interface in the RANS region as well. The turbulent viscosity increases downstream of the interface, and the peak values reached at $x/\Delta = 3.025$ are $\nu_t/\nu = 0.7 - 4.2$ (compare with the profiles presented in Figure 13 (b)).

Analyzing Figure 15, it is seen that the flow recovers quickly downstream of the interface, with a slight difference between different $f_{k,int}$ values. The friction velocity indicates that the LES flow needs only 1.5-2

boundary layer thicknesses to recover a friction velocity near unity as in the RANS region. The oscillations seen for $f_{k,int} = 0.025$ in Figure 15 (b) are present in all simulations. For all other cases, only every second node is plotted in the outlet region in order to make the figure clearer.

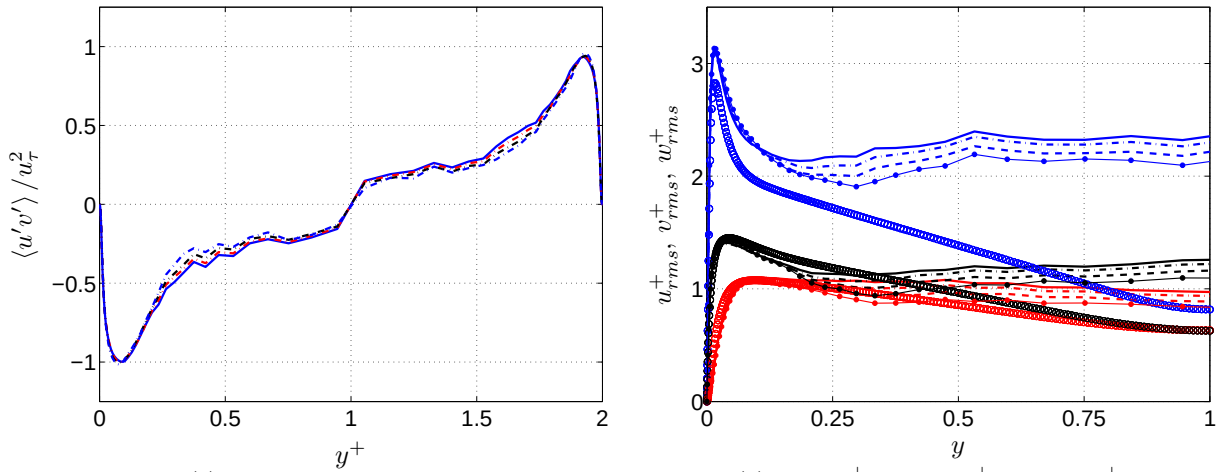

(a) Resolved shear stress.

(b) —— : u^+_{rms}; —— : v^+_{rms}; —— : w^+_{rms}

Figure 14. Channel flow using embedded LES. PDH-LRN with Δ_{dw}. (a) Time-averaged resolved shear stress at $x/\delta = 3.025$. —— : $f_{k,int} = 0.025$; - - - : $f_{k,int} = 0.050$; - - - : $f_{k,int} = 0.100$; - - - : $f_{k,int} = 0.200$. (b) Resolved turbulent fluctuations. —— : $f_{k,int} = 0.025$; - - - : $f_{k,int} = 0.050$; - - - : $f_{k,int} = 0.100$; - - - : $f_{k,int} = 0.200$. Markers are DNS data.[21] (Caption only indicates plot symbol for each $f_{k,int}$, colors indicated by figure legend.)

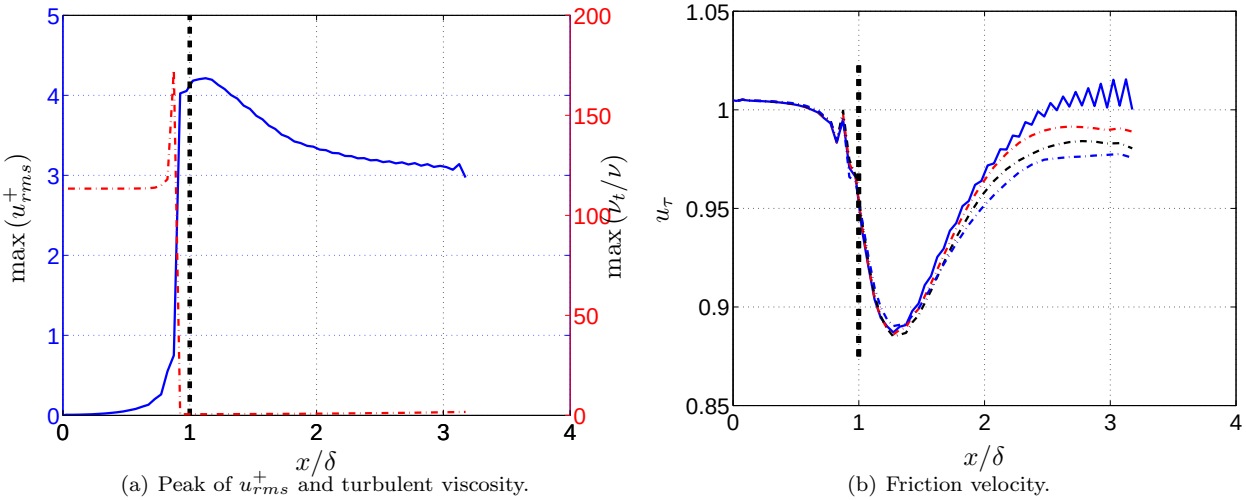

(a) Peak of u^+_{rms} and turbulent viscosity.

(b) Friction velocity.

Figure 15. Channel flow using embedded LES. PDH-LRN with Δ_{dw}. Interface indicated by dashed black line. (a) Peak of u^+_{rms} and turbulent viscosity using $f_{k,int}$=0.05. —— : peak of u^+_{rms}; - - - : peak of turbulent viscosity. (b) Friction velocity. —— : $f_{k,int} = 0.025$; - - - : $f_{k,int} = 0.050$; - - - : $f_{k,int} = 0.100$; - - - : $f_{k,int} = 0.200$.

No change in turbulent viscosity is observed in the RANS upstream of the interface. However, the values of maximum u^+_{rms} are larger than zero for $x/\delta < 1$, which indicates that the imposed fluctuations affect the RANS domain. Moreover, the effect of the imposed fluctuations in the RANS domain is also reflected in the friction velocity, which decreases when approaching the interface.

The abrupt reduction in the turbulent viscosity at the interface is a result of the modified turbulent quantities. To compensate for the reduced modeled stresses, caused by the reduction in turbulent viscosity, the resolved counter part must increase. The anisotropic synthetic turbulence is imposed to stimulate the development of the turbulence resolving flow but does not manage to increase the resolved stresses as much as needed to compensate for the, almost negligible, modeled part, and a grey area appears. The grey area is small, however. The flow recovers in only 1.5 boundary layer thicknesses as shown in Figure 15 (b).

The simulations presented show that the proposed model is well suited for use in an embedded LES framework. The overall results are in good agreement with DNS data and are comparable with other simulations of channel flow using embedded LES, e.g. by Davidson and Peng.[16] The value $f_{k,int} = 0.050$ was chosen as optimal for the studied channel flow. The location of the interface relative to the region of interest is important. In the flow case studied, the best results are given at 1.5-2 boundary-layer thicknesses downstream of the RANS-LES interface.

IV.D. Hump Flow

The hump flow is simulated using an embedded LES approach. A precursor simulation is used for the interface properties, which are the inputs to the subsequent zonal RANS-LES computation. As in the fully developed channel flow, RANS is applied in the near-wall region, and the wall-parallel RANS-LES switch is prescribed at a specific grid line. Three different locations were evaluated: $j = 26$, $j = 32$, and $j = 36$ corresponding to $y^+ = 112$, 260 and 450, where the y^+-values are computed at the interface ($x/c = 0.60$).

The Reynolds number for the hump flow is $Re_c = 936\ 000$, based on the hump length, c, and the mean inlet centerline velocity U_{cl}. In the simulations, c, ρ and U_{cl} were set to unity and the viscosity was manipulated to match the Reynolds number. The height of the hump is given by $h/c = 0.128$ and the channel height, $H/c = 0.91$. The grid used has $314 \times 120 \times 64$ cells with a spanwise cell size of $Z_{max} = 0.2$. The computational domain and the grid used, which was created by Professor Strelets group in St. Petersburg and used as the mandatory grid in the EU project Advanced Turbulence Simulations for Aerodynamic Application Challenges (ATAAC), are shown in Figure 16.

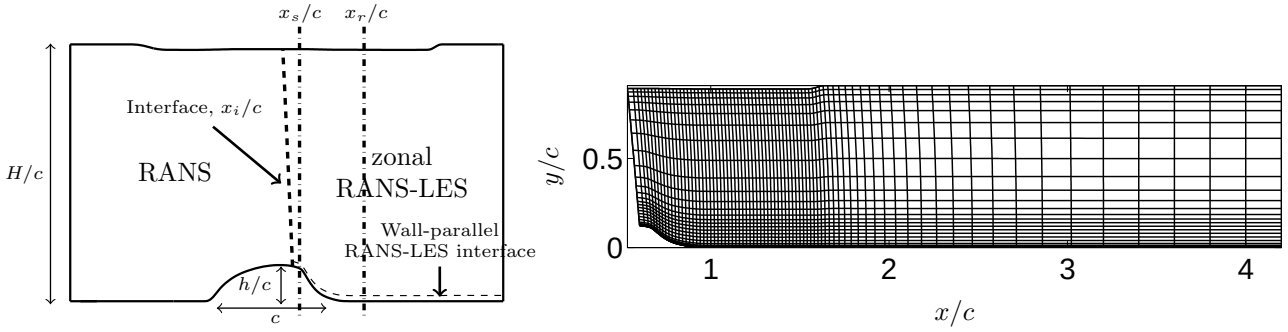

(a) Computational domain.

(b) Grid used in the simulations.

Figure 16. Hump configuration. (a) Computational domain with interfaces ($x_i/c = 0.60$), flow separation ($x_s/c = 0.65$) and re-attachment ($x_r/c = 1.1$) lines. Not to scale. (b) Computational grid used in the zonal RANS-LES simulations. Every fourth grid line is shown.

The vertical interface is located at $x/c = 0.60$, see Figure 16. Values in the range of $0.05 \leq f_{k,int} \leq 0.20$ were investigated for the interface. However, the influence was negligible for values of $f_{k,int}$ in the tested range. All the simulations presented therefore used $f_{k,int} = 0.10$.

The turbulent RANS quantities (k and ω), taken from a precursor 2D RANS computation by Professor Strelets group using Menter's SST $k-\omega$ model, were modified according to Eq. 28 and Eq. 30-32. The mean velocity field at the interface was taken from a precursor embedded LES simulation performed by ANSYS with MSST as the RANS model. Anisotropic turbulent fluctuations according to Davidson and Peng[16] were added to the mean flow field to reduce the grey area downstream of the interface (see also Section II). The Neumann condition was applied to the outflow section, which is located at $x/c = 4.2$.

For the zonal RANS-LES simulations, 95% central differencing and 5% second order upwind van Leer scheme was used to discretize the continuity and momentum equations. A blend of the two discretization schemes was motivated by a previous investigation of the hump flow by Davidson and Peng,[22] where it was shown that 100% central differencing gave unphysical fluctuations, especially in the interface region. The turbulent transport equations were discretized using a first order hybrid scheme. In the simulations 7500 time steps were run in order to establish the flow field and another 7500 time steps were done for time-averaging and data sampling. A time step of $\Delta t = 0.002$ was used.

The simulations are compared to pressure and skin friction distributions as well as velocity and shear stress profiles from experimental data by Greenblatt et al.[23,24] As a reference simulation, zonal RANS-LES based on MSST was used with a prescribed RANS-LES interface located at $y^+ = 260$ and $\Delta = \Delta_{dw}$. The

same interface conditions for k and ω were used in this simulation as for the simulation using PDH-LRN as the base model with the RANS-LES switch at $y^+ = 260$.

Side wall effects are present (three dimensional flow) due to the side plates used in the experiment. However, the side wall effects were not included in the CFD simulations since symmetry boundary conditions were used in the spanwise direction. Instead, the blockage caused by the side wall effects was computed and compensated for in the CFD simulations by modifying the upper wall, which was moved slightly downwards, see Figure 16.

Figure 17 shows the pressure and the skin friction distributions over the crest and on the lee side of the hump. The pressure and skin friction distribution are captured very well up to $x/c = 1.25$ using PDH-LRN as the base model with the switch at $y^+ = 120$. Further downstream, the predicted skin friction starts to deviate, and all PDH-LRN simulations predicts a too high skin friction at $x/c = 1.5$, indicating too strong a recovery compared to the experiment. Comparing with the simulations where the RANS-LES switch takes place at $y^+ = 260$ and 450, the predicted skin friction distributions are similar with a slightly better recovery for $y^+ = 260$. Comparing the PDH-LRN and MSST based simulations with the switch location at $y^+ = 260$, the skin friction are slightly better with MSST.

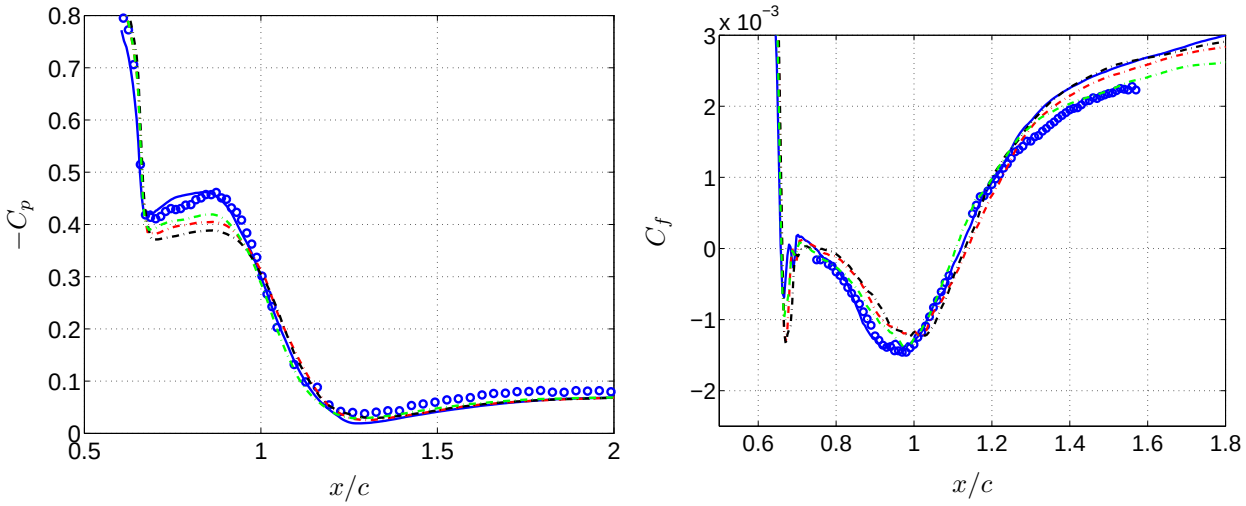

(a) Pressure. (b) Skin friction.

Figure 17. Hump flow using the PDH-LRN and MSST as base models, $f_{k,inlet} = 0.10$. Time-averaged pressure and skin friction coefficients along the bottom wall. ——: PDH-LRN, $y^+ = 112$; -·-·-: PDH-LRN, $y^+ = 260$; - - -: PDH-LRN, $y^+ = 450$; - - -: MSST, $y^+ = 260$; ○: Experiments.

The predicted velocity profiles, as shown in Figure 18, are overall in good agreement with the experimental data. At $x/c = 0.65$, the near-wall part is well predicted but the predicted velocity profiles start to deviate from the experimental data for $y > 0.135$. Moving downstream to $x/c = 0.80$, the near-wall flow is best predicted in the PDH-LRN simulation with the RANS-LES switch located at $y^+ = 120$. The prediction using MSST is in good agreement with the experimental data. For the near-wall flow, the MSST simulation behaves like the simulation using PDH-LRN with the RANS-LES switch at $y^+ = 120$, even though MSST switches further away from the wall at $y^+ = 260$. For $x/c = 1.00$ and $x/c = 1.10$, only minor differences are observed between the base models and the switch locations. As seen in the skin friction distribution, the tendency towards a too fast recovery of the flow after re-attachment is confirmed by the overprediction of the near-wall velocities at $x/c = 1.20$ and $x/c = 1.30$.

Figure 19 presents shear stress. Close to the interface at $x/c = 0.65$, the modeled part of the shear stress dominates. After the flow separation, however, the modeled shear stress is almost negligible. Only a small part is observed at $x/c = 0.80$. Comparison of the resolved shear stress between the simulations shows the result is as expected. The resolved shear stress decreases with an increased thickness of the RANS layer for the PDH-LRN based model. At $x/c = 0.80$, the properties of the free shear layer have a strong heritage from the upstream attached boundary layer, which is partly treated in RANS and thus only contains a very low level of resolved turbulence. The trend for the resolved shear stress is observed in all downstream stations.

Overall, the PDH-LRN model predicts the resolved shear stress in reasonably good agreement with experimental data. At $x/c = 0.80$ and $x/c = 1.00$, the RANS-LES switch location at $y^+ = 120$ gives the

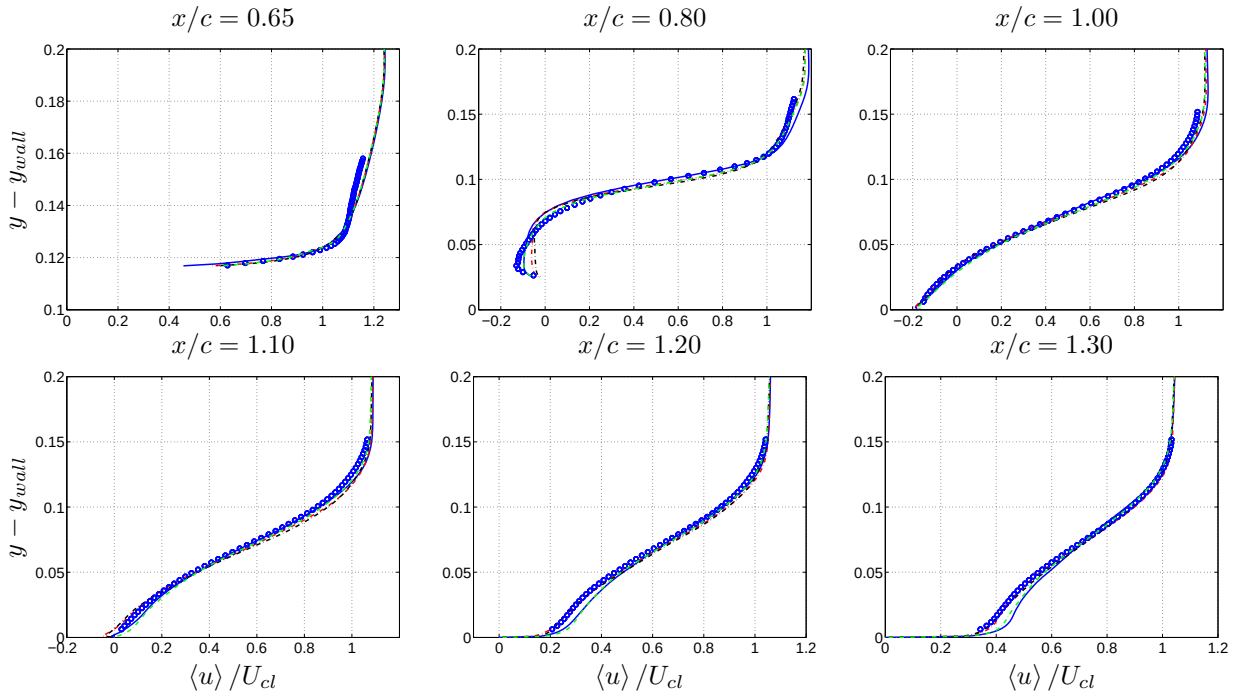

Figure 18. Hump flow using PDH-LRN and MSST as the base models, $f_{k,inlet} = 0.10$. Time-averaged streamwise velocity. ——: PDH-LRN, $y^+ = 112$; -·-·-: PDH-LRN, $y^+ = 260$; - - -: PDH-LRN, $y^+ = 450$; -·-·-: MSST, $y^+ = 260$; ○: Experiments.

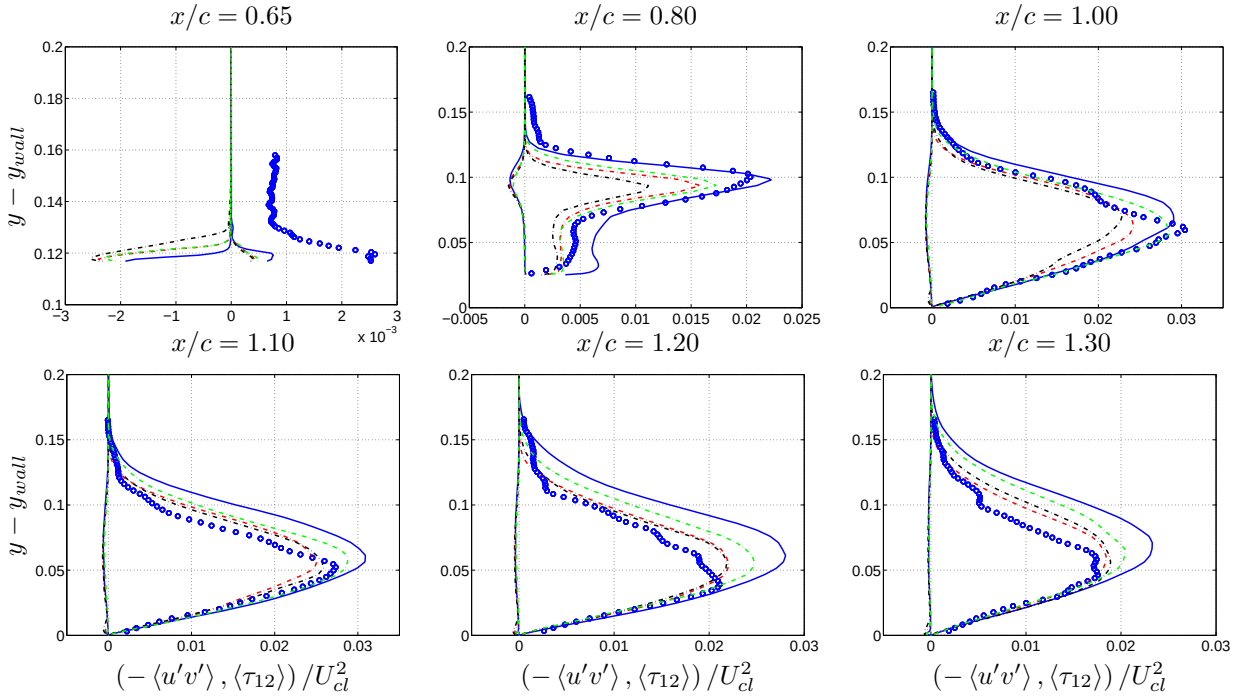

Figure 19. Hump flow using PDH-LRN and MSST as the base models, $f_{k,inlet} = 0.10$. Time-averaged shear stress. ——: PDH-LRN, $y^+ = 112$; -·-·-: PDH-LRN, $y^+ = 260$; - - -: PDH-LRN, $y^+ = 450$; -·-·-: MSST, $y^+ = 260$; ○: Experiments.

best agreement with experimental data. For the locations downstream of $x/c = 1.00$, the switch location at $y^+ = 120$ overpredicts the resolved shear stress, and the PDH-LRN simulations using the switch locations at $y^+ = 260$ and $y^+ = 450$ give better agreement with the experimental data. The more accurately resolved shear stress is also reflected in the better predicted velocity profiles, as seen in Figure 18. The overprediction of resolved shear stress gives an under-estimation of the bubble size.

A distinct reduction in the turbulent viscosity, as seen in fully developed channel flow, is also observed

when switching from RANS to LES in the hump flow, which is seen in Figure 20. No large differences are present in the SGS turbulent viscosity predicted with PDH-LRN as the base model. It is observed that MSST predicts lower levels of SGS turbulent viscosity than the PDH-LRN model. In the RANS region at $x/c = 0.65$, the turbulent viscosities are comparable in MSST and PDH-LRN with the switch at $y^+ = 260$. However, at the downstream stations, MSST predicts much lower turbulent viscosity levels compared to PDH-LRN. The levels of turbulent viscosity in MSST with the switch at $y^+ = 260$ are comparable with the levels given by PDH-LRN with the switch at $y^+ = 120$. The differences between the two base models are hence clearer in the hump flow than in the fully developed channel flow presented in the above section.

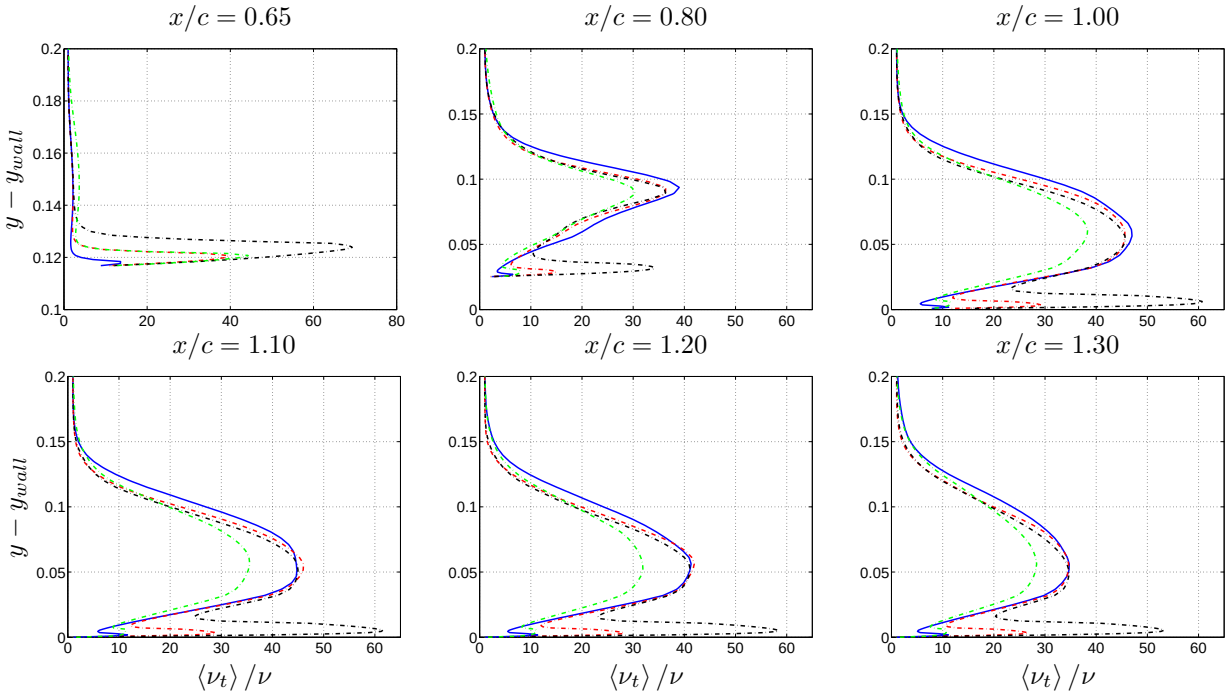

Figure 20. Hump flow using PDH-LRN and MSST as the base models, $f_{k,inlet} = 0.10$. Time-averaged turbulent viscosity. —— : PDH-LRN, $y^+ = 112$; - - - : PDH-LRN, $y^+ = 260$; - - - : PDH-LRN, $y^+ = 450$; - - - : MSST, $y^+ = 260$.

V. Summary and Concluding Remarks

An improved hybrid RANS-LES model has been proposed based on a Low-Reynolds-Number $k - \omega$ model (PDH-LRN). The turbulence resolving mode has been calibrated in Decaying Homogeneous Isotropic Turbulence, giving $C_{LES} = 0.70$. Moreover, the model has been applied to fully developed channel flow at $Re_\tau = 8000$ using a zonal RANS-LES approach. Four different prescribed RANS-LES switch locations were evaluated together with four different LES length scales. A LES length scale based on the wall distance and the maximum local cell size, Δ_{dw}, was concluded to give the best results regarding a reduction of log-layer mismatch. The length scale gives a substantial reduction in turbulent viscosity at the RANS-LES interface, which has led, as desired, to a quick increase of resolved turbulence and thus reducing the log-layer mismatch.

An embedded LES approach was used in channel flow and hump flow with the proposed model in order to demonstrate and evaluate a RANS-LES interface methodology where the convective and diffusive fluxes of the turbulent quantities are modified and anisotropic turbulence are added to the oncoming RANS mean flow field. The results produced for fully developed channel flow, the channel flow of embedded LES and the hump flow are in reasonably good agreement with DNS or experimental data. Zonal RANS-LES simulations based on Menter's SST $k - \omega$ were used as reference.

Simulations using the proposed model give higher turbulent viscosities than simulations based on MSST. This is clear in the RANS region, especially for the hump flow. The same tendency has been observed in turbulence resolving flow using LES but has not been seen to be as significant as in the RANS region. In fully developed channel flow, it was observed that the higher levels of turbulent viscosity produced with the PDH-LRN base model are an advantage as compared to the lower levels produced with MSST in terms of reducing the log-layer mismatch.

The higher RANS turbulent viscosity in combination with the wall distance based LES length scale gave superior results in comparison with classical LES length scales, such as the local maximum cell size or the cube root of the local control volume. Moreover, the RANS-LES switch location affects the level of the log-layer mismatch and is dependent on which LES length scale is used. Using Δ_{dw} as the LES length scale, a weak effect was observed for different switch locations. However, a much stronger effect was observed using the LES length scale based on local maximum cell size, Δ_{max}, where the log-layer mismatch increases when the RANS-LES interface is moved closer to the wall. For a RANS-LES switch location at $y^+ = 250$, an underprediction of 13.7% in skin friction is given with Δ_{max} compared to the log-law, while Δ_{dw} only gives an underprediction of 1.8%.

Acknowledgments

This work was funded by the Swedish National Aviation Engineering Research Program (NFFP). The authors would like to acknowledge the financial support of VINNOVA and Saab Aeronautics. The EU-project ATAAC (Advanced Turbulence Simulations for Aerodynamic Application Challenges), in which Saab Aeronautics has been an observer and Chalmers and FOI have been partners, is also acknowledged. Moreover, the financial support of SNIC (Swedish National Infrastructure for Computing) for computer time at NSC (National Supercomputer Center) and C^{3}SE (Chalmers Center for Computational Science and Engineering) is gratefully acknowledged.

References

[1]Peng, S.-H., Davidson, L., and Holmberg, S., "A Modified Low-Reynolds-Number $k-\omega$ Model for Recirculating Flows," *Journal of Fluids Engineering*, Vol. 119, 1997, pp. 867–875.

[2]Arvidson, S., Peng, S.-H., and Davidson, L., "Feasibility of Hybrid RANS-LES of Shock/Boundary-Layer Interaction in a Duct," *Progress in Hybrid RANS-LES Modelling*, edited by F. S. et al., Vol. 117 of *NNFM*, Springer, 2012, pp. 245–256.

[3]Spalart, P., Jou, W.-H., Strelets, M., and Allmaras, S., "Comments on the Feasability of LES for Wings, and on a Hybrid RANS/LES Approach," *Advances in DNS/LES*, Ruston, Lousiana, 1997, pp. 137–147.

[4]Breuer, M., Joicic, N., and Mazaev, K., "Comparison of DES, RANS and LES for the separated flow around a flat plate at high incidence," *International Journal for Numerical Methods in Fluids*, Vol. 41, 2003, pp. 357–388.

[5]Spalart, P., "Detached-Eddy Simulation," *Annual Review of Fluid Mechanics*, Vol. 41, 2009, pp. 181–202.

[6]Davidson, L. and Peng, S.-H., "Hybrid LES-RANS modelling: a one-equation SGS model combined with a $k-\omega$ model for predicting recirculating flows," *International Journal for Numerical Methods in Fluids*, Vol. 43, 2003, pp. 1003–1018.

[7]Chauvet, N., Deck, S., and Jaquin, L., "Zonal Detached Eddy Simualtion of a Controlled Propulsive Jet," *AIAA Journal*, Vol. 45, 2007, pp. 2458–2473.

[8]Deck, S., "Recent improvments in the Zonal Detached Eddy Simualtion (ZDES) formulation," *Theoretical and Computational Fluid Dynamics*, 2011.

[9]Spalart, P., Deck, S., Shur, M., Squires, K., Strelets, M. K., and Travin, A., "A new version of detached-eddy simulation, resistant to ambiguous grid densities," *Theory of Computational Fluid Dynamics*, Vol. 20, 2006, pp. 181–195.

[10]Shur, K., Spalart, P., Strelets, M., and Travin, A., "A hybrid RANS-LES approach with delayed-DES and wall-modelled LES capabilities," *International Journal of Heat and Fluid Flow*, Vol. 29, 2008, pp. 1638–1649.

[11]Wilcox, C. W., "Simulation of Transition with a Two-Equation Turbulence Model," *AIAA Journal*, Vol. 32, 1994, pp. 247–255.

[12]Menter, F., "Two-Equation Eddy-Viscosity Turbulence Models for Engineering Applications," *AIAA Journal*, Vol. 32, 1994, pp. 1598–1605.

[13]Strelets, M., "Detached Eddy Simulation of Massively Separated Flows," AIAA 2001-0879, Reno, Nevada, 2001.

[14]Mocket, C., *A comprehensive study of detached-eddy simulation*, Ph.D. thesis, der Technischen Universität Berlin, 2009.

[15]Arvidson, S., "Assessment and Some Improvements of Hybrid RANS-LES Methods," Licenciate thesis ISSN 1652-8565, 2013:01, Applied Mechanics, Chalmers University of Technology, 2013.

[16]Davidson, L. and Peng, S.-H., "Embedded Large-Eddy Simulation Using the Partially Averaged Navier-Stokes Model," *AIAA Journal*, Vol. 51, 2013, pp. 1066–1079.

[17]Emvin, P., *The full multigrid method applied to turbulent flow in ventilated enclosures using structured and unstructured grids*, Ph.D. thesis, Chalmers University of Technology, 1997.

[18]Comte-Bellot, G. and Corrsin, S., "Simple Eularian Time Correlation of Full- and Narrow-Band Velocity Signals in Grid-Generated "Isotropic" Turbulence," *Journal of Fluid Mechanics*, Vol. 48, No. 2, 1971, pp. 273–337.

[19]Bunge, U., Mockett, C., and Thiele, F., "Calibration of different models in the context of detached-eddy simulation," Arbetisgemeinschaft "Strömmungen mit Ablösung" STAB Jahersbericht, 2003.

[20]Nikitin, N., Nicoud, F., Wasistho, B., Squires, K., and Spalart, P., "An approach to wall modeling in large-eddy simulations," *Physics of Fluids*, Vol. 12, 2000, pp. 1629–1632.

[21]Hoyas, S. and Jimenez, J., "Reynolds number effects on the Reynolds-stress budgets in turbulent channels," *Physics of Fluids A*, Vol. 20, 2008, pp. 101511.

[22]Davidson, L. and Peng, S.-H., "Embedded LES Using PANS," *6th AIAA Theoretical Fluid Mechanics Conference, AIAA-2011-3108*, Honolulu, Hawaii, 2011.

[23]Greenblatt, D., Paschal, K., Yao, C.-S., Harris, J., Schaeffler, N. W., and Washburn, A. E., "A Separation Control CFD Validation Test Case Part 1: Baseline & Steady Suction," AIAA 2004-2220, Portland, OR, 2004.

[24]Greenblatt, D., Paschal, K., Yao, C.-S., and Harris, J., "A Separation Control CFD Validation Test Case Part 2: Zero Efflux Oscillatory Blowing," AIAA 2005-0485, Reno, OR, 2005.